Amorphization of rare earth - cobalt intermetallic alloys by swift heavy-ion irradiation

1996 J. Phys.: Condens. Matter 8 8191

(http://iopscience.iop.org/0953-8984/8/43/015)

J. Phys.: Condens. Matter **8** (1996) 8191–8206. Printed in the UK

Amorphization of rare earth–cobalt intermetallic alloys by swift heavy-ion irradiation

M Ghidini†‡, J P Nozières†, D Givord†, M Toulemonde§ and B Gervais§

† Laboratoire L Néel, CNRS, 38042 Grenoble Cedex, France
§ CIRIL, CEA/CNRS, Caen Cedex, France

Received 19 June 1996

Abstract. RCo_2 (R = Y, Ce and Tm) and RCo_3 (R = Y and Ce) intermetallic compounds have been irradiated for the first time by swift heavy-ion beams (U, Pb) of energy 1–5 GeV at GANIL (Caen, France). The compounds YCo_2, $CeCo_3$ and YCo_3 are found to be partially amorphized after irradiation. The amorphized volume fraction has been determined as a function of the ion beam fluence by x-ray diffraction and magnetic measurements. Results are found to be in agreement. By means of a phenomenological model, associating the phenomena of amorphization and recrystallization, the diameters of the latent tracks are estimated to lie in the range 2–3 nm. In contrast, no amorphization is observed in $CeCo_2$ and $TmCo_2$. The different behaviours observed are well understood, in the framework of the thermal spike model, in terms of the different values of the electron–phonon coupling constant of the irradiated compounds.

1. Introduction

An energetic ion passing through a solid can be slowed down either through elastic scattering with the target atoms (nuclear energy loss or nuclear stopping power, $S_n = -\mathrm{d}E/\mathrm{d}x$) or through inelastic scattering with the target electrons (electronic energy loss or electronic stopping power, $S_e = -\mathrm{d}E/\mathrm{d}x$). In the case of swift heavy-ion–solid interactions S_n can be neglected with respect to S_e.

It is well known that heavy-ion irradiation in the electronic stopping power regime (namely $S_e \gg S_n$) can induce damage in insulating materials. In several cases, latent tracks are observed. These are extended columnar defects, with a quite regular cylindrical shape. Latent tracks have been shown to be amorphous, with diameters of a few nanometres [1].

Recent studies have shown that structural modifications can also be induced in metals by swift heavy-ion irradiation. The first damage effect which has been ascribed to the electronic stopping power was the annealing under irradiation of Frenkel pairs previously induced by elastic collisions in Ni [2]. Similar effects have later been reported to occur in Fe and Ni_3Fe [3]. Since very-high-energy ion accelerators have been developed, the sensitivity of pure metals and alloys to swift heavy-ion irradiation has been extensively tested for very high values of the electronic stopping power. Most of the pure metals (Cu, Nb, Pd, Ag, W and Pt) have been found to be insensitive [4, 5]. In contrast, the formation of aggregates of point defects has been reported in irradiated Ti [6].

Until now, only a few examples of structural phase transformations or amorphization induced by swift heavy-ion irradiation have been demonstrated in metallic materials. In

‡ Present address: Istituto MASPEC del CNR, via Chiavari 18/A, 43100 Parma, Italy.

0953-8984/96/438191+16$19.50

the NiTi alloy, which crystallizes in the monoclinic structure at room temperature, the coexistence of the cubic phase (normally stable at high temperature), the monoclinic phase and the amorphous phase is observed after irradiation [7]. Amorphization of the Ni_3B alloy is observed by electron diffraction [8]. In both cases, the precipitation of latent tracks has been deduced by indirect methods. To the best of our knowledge, the only direct observation of latent tracks in metallic materials was in the $NiZr_2$ alloy [9].

In order to investigate the potential of heavy-ion irradiation as a technique for preparing nanostructured magnetic systems, RCo_2 (R = Y, Ce and Tm) and RCo_3 (R = Y and Ce) intermetallic alloys have been irradiated for the first time by swift heavy-ion beams [10]. These compounds were chosen for their property of being magnetic in the amorphous state and non-magnetic or weakly magnetic in the crystalline state. Thus, the basic idea was to create amorphous magnetic nanoparticles (the latent tracks) embedded in the residual crystalline non-magnetic matrix. The YCo_3 alloy, which is strongly ferromagnetic both in the crystalline state and in the amorphous state, has been irradiated in order to obtain a heterogeneous magnetic material constituted by a mixing, at the nanometric scale, of a hard phase (the residual crystalline matrix) and a soft phase (the irradiation-induced amorphous tracks). In the field of magnetic materials research, such systems are currently object of extended investigation [11]. Magnetic nanoparticles have been prepared by swift heavy-ion irradiation. Their nanometric size allowed original magnetic properties and processes to be demonstrated [12–14].

This paper shall focus on the characterization of the irradiation-induced damage in the intermetallic compounds RCo_2 and RCo_3 by means of x-ray diffraction and magnetic measurements. Emphasis is given to the microscopic mechanisms of damage creation in such compounds. The different behaviours observed after irradiation are explained in terms of a transient thermal process (thermal spike) and ascribed to the different strength of the electron–phonon coupling in the considered compounds. Results are found to be in agreement with experiment.

2. Experimental

RCo_2 (R = Y, Ce and Tm) and RCo_3 (R = Y and Ce) films with thicknesses of around 1 μm have been deposited by DC sputtering with a deposition pressure of 10^{-3} Torr. With the exception of $CeCo_2$ films, which were directly crystallized during deposition, the as-deposited films were amorphous. Crystallization of the cubic Laves phase (YCo_2 and $TmCo_2$) or of a hexagonal phase ($YCo_3$and $CeCo_3$) was obtained by post-deposition heat treatments at 500–600°C during 1 h. Compositions and thicknesses were determined by x-ray fluorescence analysis and SEM. X-ray diffraction and transmission electron microscopy revealed the crystallized films to be isotropic polycrystals with an average grain size of 100–200 Å.

The crystalline samples were then irradiated at GANIL (Caen, France), by 1 GeV U or 5 GeV Pb ion beams, on the medium-energy line (ME) or on the high-energy line (HE) respectively. The penetration depths, the nuclear and the electronic stopping powers were calculated for all the compounds by using a TRIM code [15]. For ion energies greater than 0.1 GeV, the nuclear stopping power was found to be negligible with respect to the electronic one in all the compounds under study. The ion penetration depths were found to be 25 and 100 μm for 1 GeV U and 5 GeV Pb beams respectively. Since the thicknesses of the samples were much smaller than the ion penetration depths, it is reasonable to expect the ions' energy loss to remain constant throughout the film thicknesses. In principle, this should ensure that the induced damage will be homogeneous along the ion paths.

X-ray diffraction and magnetic measurements were used to investigate the irradiated samples. X-ray diffraction measurements were performed with a θ–2θ diffractometer. Magnetic measurements were performed using either VSM or SQUID magnetometers.

3. Experimental results

3.1. YCo_2

YCo_2 is ferromagnetic in the amorphous state, but it is a Pauli paramagnet in the crystalline state [16]. The as-deposited amorphous samples have been found to be ferromagnetic (figure 1b) with a saturation magnetization of 360 emu cm^{-3}, corresponding to a saturation magnetic moment $\mu_s = 1\mu_B$/Co, in good agreement with the value for amorphous YCo_2 reported in the literature [16]. After heat treatment, only a negligible residual magnetic signal (5 emu cm^{-3}) was measured in the crystallized YCo_2 samples [13].

The crystalline samples were irradiated at room temperature by 1 GeV ^{238}U ions. Fluences of 10^{12}, 5×10^{12} and 1.8×10^{13} ions cm^{-2} were achieved.

Figure 1(a) shows a detailed view of the 311 and 222 reflections of the irradiated samples. The same reflections for the non-irradiated sample are also shown for reference. The peak's intensity lowers as the beam fluence is increased, indicating that a progressive loss of crystallinity occurs.

Figure 1(b) shows the thermal variation of the magnetization measured in a constant field $H = 10$ kOe for the irradiated samples, compared to that of the fully amorphous YCo_2 sample. The magnetization progressively increases with fluence. The Curie temperature of the irradiated samples can be located at 150 K; that is, it is strongly reduced with respect to the fully amorphous YCo_2 sample. This effect has been ascribed to the low dimensionality of the nanoparticles [12]. That interpretation has been confirmed by ferromagnetic resonance measurements [17] .

The results obtained by x-ray diffraction and magnetic measurements are consistent with the stabilization of amorphous regions in the residual crystalline matrix of the irradiated samples. The amorphized volume fraction $p_a(\Phi) = v_a/V_t$, where v_a is the amorphized volume and V_t is the total volume of the film, has been determined by (i) x-ray diffraction measurements by taking the ratio of the YCo_2 peak integrated intensities measured prior to and after irradiation ($p_a(\Phi) = 1 - I(\Phi)/I(0)$) and (ii) by magnetic measurements by taking the ratio between the low-temperature magnetization induced by irradiation and the low-temperature magnetization of the fully amorphous sample ($p'_a(\Phi) = M_s(\Phi)/M_s^{(a)}$). A good agreement is found between $p_a(\Phi)$ and $p'_a(\Phi)$ (figure 2); the saturation magnetic moment in the irradiated samples is found to be in agreement with the value for amorphous YCo_2.

The amorphized volume fraction versus fluence saturates before the total amorphization of the sample is achieved. If one assumes that the amorphous regions are associated to the ion tracks, this can be understood in terms of an exclusion volume surrounding each track. The exclusion volume defines a minimum distance between the tracks, so that no overlap can occur. In this picture, each incoming ion would have two effects on the crystalline matrix: (i) the creation of an amorphous track and (ii) the recrystallization of every pre-existing track inside the exclusion volume. Therefore, the kinetics of defects creation can be described by

$$\frac{\mathrm{d}p_a}{\mathrm{d}\Phi} = \sigma_a[1 - p_a(\Phi)] - \sigma_r p_a(\Phi) \qquad (1a)$$

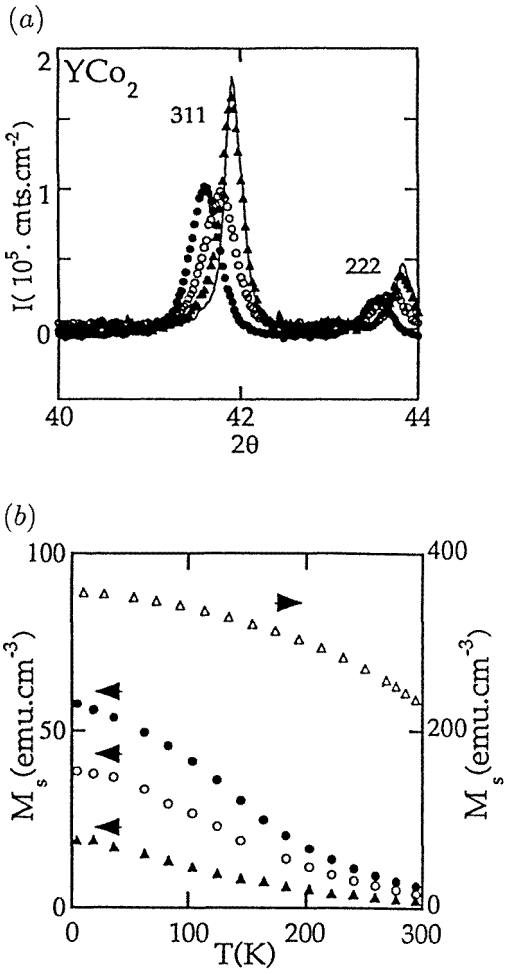

Figure 1. (a) A detailed view of the most intense (311) and (222) reflections for the samples of YCo_2 irradiated by 10^{12} ions cm^{-2} (full triangles), 5×10^{12} ions cm^{-2} (open circles) and 1.8×10^{13} ions cm^{-2} (full circles); the same reflections are also shown for the non-irradiated sample (full line). (b) The thermal variation of the magnetization in a field $H = 10$ kOe for the samples irradiated at 10^{12} ions cm^{-2} (full triangles), 5×10^{12} ions cm^{-2} (open circles) and 1.8×10^{13} ions cm^{-2} (full circles); the thermal variation of the magnetization of the fully amorphous YCo_2 sample (open triangles) is also shown for reference.

$$\frac{\mathrm{d}p_r}{\mathrm{d}\Phi} = \sigma_r[1 - p_r(\Phi)] - \sigma_a p_r(\Phi) \tag{1b}$$

with the normalization condition $p_a(\Phi) + p_r(\Phi) + p_c(\Phi) = 1$. $p_a(\Phi)$ is the amorphized volume fraction, $p_r(\Phi)$ is the recrystallized volume fraction and $p_c(\Phi)$ is the virgin crystalline volume fraction; σ_a and σ_r are the amorphization and recrystallization cross sections respectively. The solution of (1) is

$$p_a(\Phi) = \frac{\sigma_a}{\sigma_a + \sigma_r}(1 - \mathrm{e}^{-(\sigma_a+\sigma_r)\Phi}) \tag{2a}$$

$$p_r(\Phi) = \frac{\sigma_r}{\sigma_a + \sigma_r}(1 - \mathrm{e}^{-(\sigma_a+\sigma_r)\Phi}). \tag{2b}$$

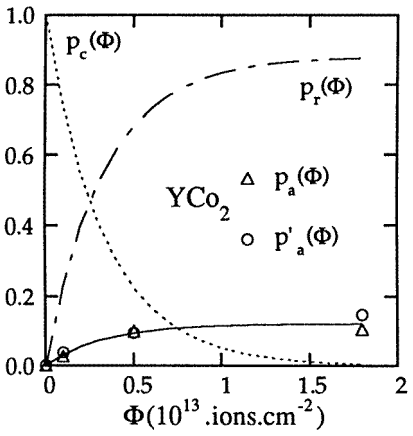

Figure 2. The full line is the best fit of the experimental values $p_a(\Phi)$ and $p'_a(\Phi)$ with equation (2*a*); the broken line is the recrystallized volume fraction calculated with equation 2(*b*); the dotted line is the residual crystalline matrix volume fraction calculated from the normalization condition $p_a(\Phi) + p_r(\Phi) + p_c(\Phi) = 1$.

Equation (2*a*) has been used to fit the experimental data, allowing σ_a and σ_r to be determined ($\sigma_a = 0.36 \times 10^{-13}$ cm^2 and $\sigma_r = 2.62 \times 10^{-13}$ cm^2). The track and exclusion volume diameters can be estimated from σ_a and σ_r respectively, by assuming the tracks to be continuous throughout the film thickness. This strong assumption is justified by the fact that the magnetic properties observed in the irradiated samples are consistent with those expected for an array of almost ideal infinite magnetic cylinders [12]. Thus

$$\sigma_a = \frac{\pi D_1^2}{4} \qquad \sigma_r = \frac{\pi (D_2^2 - D_1^2)}{4} \tag{3}$$

where D_1 and D_2 are the diameters of the amorphous tracks and of the exclusion volume respectively. The values $D_1 = 21$ Å and $D_2 = 61$ Å are found.

In figure 1(a), the peak positions are progressively shifted towards smaller Bragg angles for increasing fluence. Grazing incidence x-ray diffraction measurements have shown the peaks' shift to be due to the anisotropic stresses developed in the plane of the sample by the amorphous tracks [18].

HRTEM observations have been performed on the irradiated samples. However, no direct observation of the ion tracks has been obtained. Small-angle neutron scattering experiments are in progress. Small-angle scattering of neutrons or x-rays are valuable tools for determining the tracks diameter in those samples in which imaging contrast between amorphous and crystalline regions is difficult to obtain [19, 20].

3.2. $CeCo_3$

The as-deposited amorphous samples are ferromagnetic up to room temperature (figure 3(b)), with a saturation magnetic moment $\mu_s = 1.5\mu_B$/Co, in good agreement with the value found in the literature for amorphous $CeCo_3$ [21]. In the heat-treated samples it is found that $\mu_s = 0.24\mu_B$/Co and the Curie temperature is 80 K (figure 3(b)). These values are in agreement with those reported for crystalline $CeCo_3$ [22].

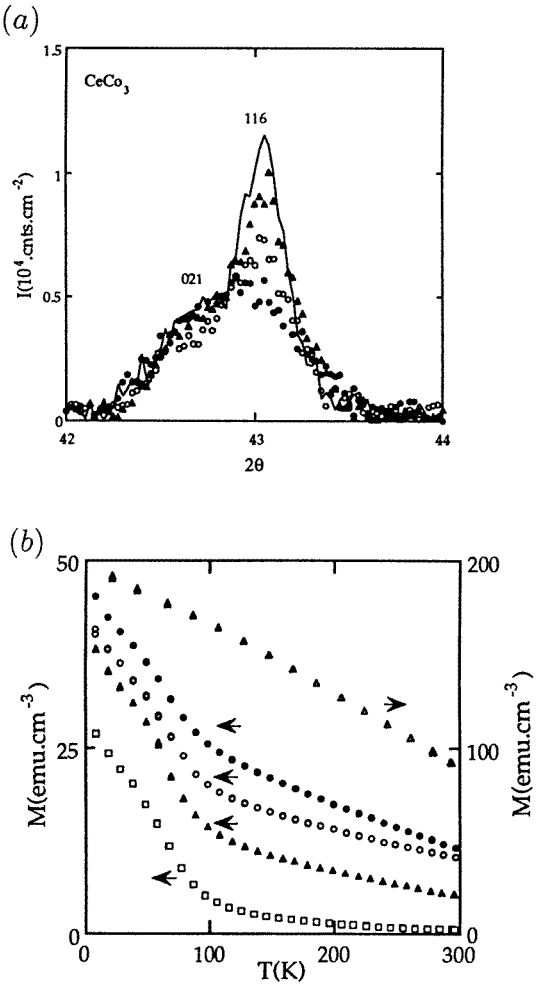

Figure 3. (a) A detailed view of the most intense $CeCo_3$(021) and (116) reflections for the non-irradiated sample (full line), and for the samples irradiated at 10^{12} ions cm^{-2} (full triangles), 5×10^{12} ions cm^{-2} (open circles) and 10^{13} ions cm^{-3} (full circles). (b) The thermal variation of the magnetization measured in a field $H = 10$ kOe for the non-irradiated sample (open squares), for the samples irradiated at 10^{12} ions cm^{-2} (full triangles), 5×10^{12} ions cm^{-2} (open circles), 10^{13} ions cm^{-2} (full circles) and for the fully amorphous sample (open triangles).

The crystalline samples were irradiated at room temperature by 5 GeV ^{208}Pb ion beams. The fluences of 10^{12}, 5×10^{12} and 10^{13} ions cm^{-2} were achieved. Figure 3(a) shows a detailed view of the most intense reflections for the irradiated samples. The same reflections for the non-irradiated sample are also shown for reference. The intensities decrease as the ion beam fluence is increased.

Figure 3(b) shows the thermal variation of the magnetization measured in a constant field $H = 10$ kOe for the irradiated samples compared to those of the fully amorphous sample and of the crystalline non-irradiated sample. The low-temperature magnetization is increased versus fluence. The magnetization of the irradiated samples undergoes a transition at around 80 K, but the samples remain magnetic up to room temperature. This behaviour

can be ascribed to the coexistence of two magnetic phases in the irradiated samples: the residual crystalline matrix and the amorphous $CeCo_3$ phase induced by irradiation. The amorphized volume fractions were determined in the same way as for the YCo_2 samples. $p'_a(\Phi)$ was determined above 100 K, at which the residual crystalline matrix is not magnetic. Results were found to be in agreement with $p_a(\Phi)$ (figure 4). Above 100 K, the saturation magnetic moment in the irradiated samples was found to be in agreement with the value reported for amorphous $CeCo_3$.

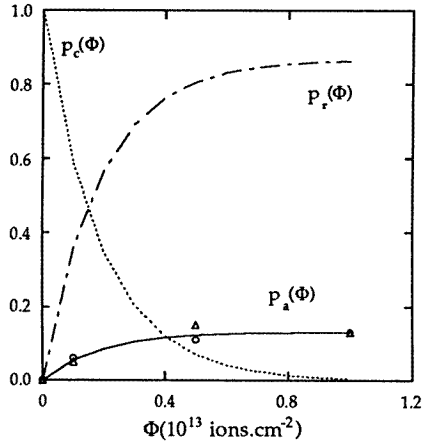

Figure 4. The full line is the best fit of the experimental values $p_a(\Phi)$ and $p'_a(\Phi)$ with equation (2*a*); the broken line is the recrystallized volume fraction calculated with equation (2*b*); the dotted line is the residual crystalline matrix volume fraction calculated from the normalization condition $p_a(\Phi) + p_r(\Phi) + p_c(\Phi) = 1$. The same symbols as in figure 2 are used for $p_a(\Phi)$ and $p'_a(\Phi)$.

As in the YCo_2 samples, the amorphized volume fraction versus fluence saturates before complete amorphization is achieved. Thus, the same phenomenological model for the kinetics of defect creation can be applied here. The estimated values for the track and exclusion volume diameters are $D_1 = 30$ Å and $D_2 = 77$ Å respectively. A detailed analysis of the magnetic properties of the irradiated samples will be presented elsewhere [23].

3.3. YCo_3

The crystalline samples were irradiated at room temperature by 5 GeV ^{208}Pb ion beams. The fluences of 10^{12}, 5×10^{12} and 10^{13} ions cm^{-2} were achieved. Figure 5 shows a detailed view of the most intense reflections for the irradiated samples. The same reflections for the non-irradiated sample are also shown for comparison. A progressive lowering of the peaks' intensity is observed when the fluence is increased. The sample irradiated at 5×10^{12} ions cm^{-2} showed a slightly different crystalline texture with respect to the other samples; the reasons for such a behaviour remain unclear. Therefore, $p_a(\Phi)$ could be carefully determined by x-ray diffraction measurements only for the samples irradiated at 10^{12} and 10^{13} ions cm^{-2} ($p_a(\Phi) = 0.04$ and $p_a(\Phi) = 0.15$ respectively). The amorphized volume fraction could not be determined by magnetic measurements since both crystalline and amorphous YCo_3 are magnetic above room temperature [24] and the two phases are

exchange-coupled in the irradiated samples because of the small size of the amorphous tracks. The track diameters cannot be estimated with equation (2*a*) because of the small number of experimental points. However, for the same irradiation fluences, $p_a(\Phi)$ is of the same order of magnitude as in the YCo_2 and $CeCo_3$ samples. It is therefore reasonable to expect the track diameter to be of the same order of magnitude as in the YCo_2 and $CeCo_3$ samples.

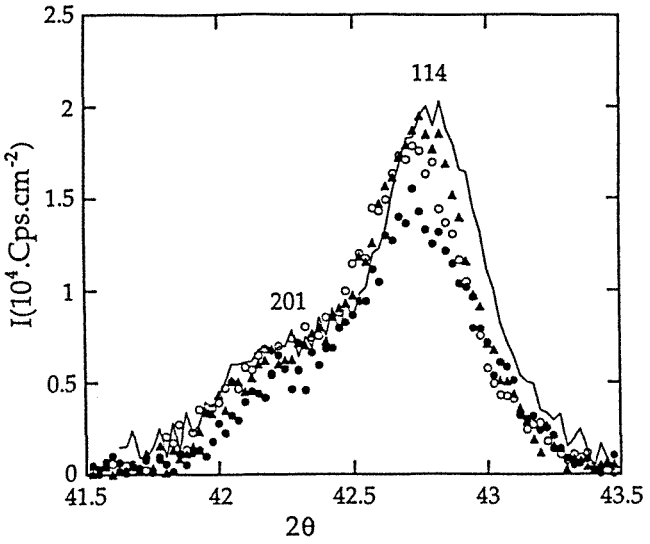

Figure 5. A detailed view of the most intense YCo_3 114 and 201 reflections for the non-irradiated sample (full line), and for the samples irradiated at 10^{12} ions cm^{-2} (full triangles), 5×10^{12} ions cm^{-2} (open circles) and 10^{13} ions cm^{-3} (full circles).

3.4. $CeCo_2$

Crystallization of the $CeCo_2$ cubic Laves phase was obtained directly during sputter deposition. Crystalline $CeCo_2$ is a Pauli paramagnet. Amorphous $CeCo_2$ is ferromagnetic with $\mu_s = 0.12\mu_B$/Co [21]. During deposition, a small fraction of Co atoms was substituted by ^{57}Fe, in order to perform a Mössbauer study on the irradiated samples. A small ferromagnetic signal ($\mu_s = 0.04\mu_B$/Co) is indeed observed at low temperature in the crystalline as-deposited samples (figure 6(b)). This value is in agreement with those reported for the $Ce(Fe_xCo_{1-x})_2$ compounds with $x \leqslant 0.1$ [25]. This composition has been also confirmed by x-ray fluorescence analysis. The samples were irradiated at room temperature by 5 GeV ^{208}Pb beams. Fluences of 10^{12}, 5×10^{12} and 10^{13} ions cm^{-2} have been achieved. Figure 6(a) shows a detailed view of the 311 and 222 reflections for the irradiated samples. The same reflections for the non-irradiated sample are also shown for reference. A splitting of the 311 reflection towards the region of smaller Bragg angles (figure 6(a)) is observed in the irradiated samples. The overall intensity of the two splitted peaks remains constant versus fluence and approximatively equal to the 311 intensity of the non-irradiated sample. This suggests that no loss of crystallinity occurs.

Figure 6(b) shows the thermal variation of the magnetization measured in a constant field $H = 10$ kOe for the irradiated samples compared to that of the non-irradiated sample.

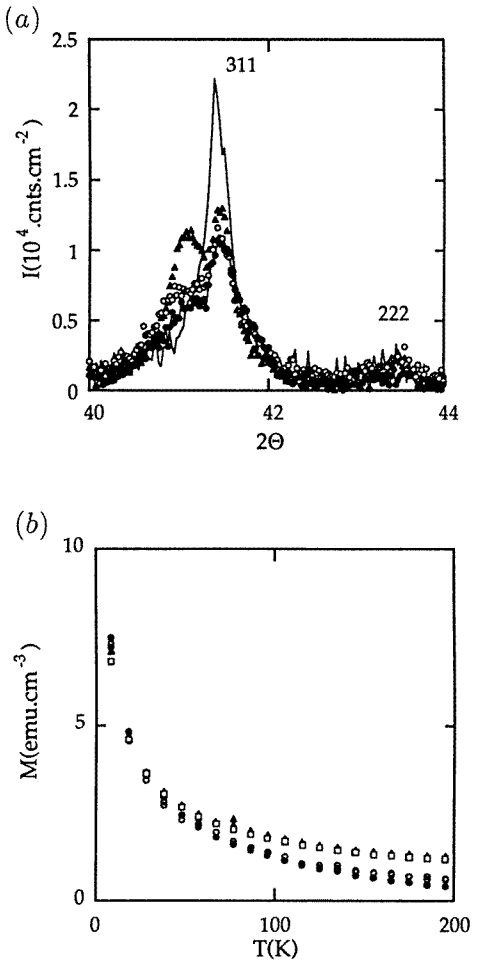

Figure 6. (a) A detailed view of the $CeCo_2$ 311 and 222 reflections for the samples irradiated at 10^{12} ions cm^{-2} (full triangles), 5×10^{12} ions cm^{-2} (open circles) and 10^{13} ions cm^{-2} (full circles); compared with those of the non-irradiated sample (full line). (b) Thermal variation of the magnetization measured in a field $H = 10$ kOe for the samples irradiated at 10^{12} ions cm^{-2} (full triangles), 5×10^{12} ions cm^{-2} (open circles) and 10^{13} ions cm^{-2} (full circles) and for the non-irradiated samples (open squares).

No significant modification is observed either in the low-temperature magnetization or in the Curie temperature. Thus, these results confirm, in agreement with x-ray diffraction measurements, that no amorphization has been induced by irradiation.

In contrast, irradiation seems to have induced the stabilization of a new crystallographic phase, which has not been identified yet. The new phase could be associated with a tetragonal or with an orthorhombic distortion of the original cubic lattice, or with the stabilization of a different cubic phase with a slightly increased lattice parameter. In this regard, it would be interesting to check whether the observed distortions of the original lattice could be associated with irradiation-induced variations of the Ce atoms' valence state. Further investigation is in progress.

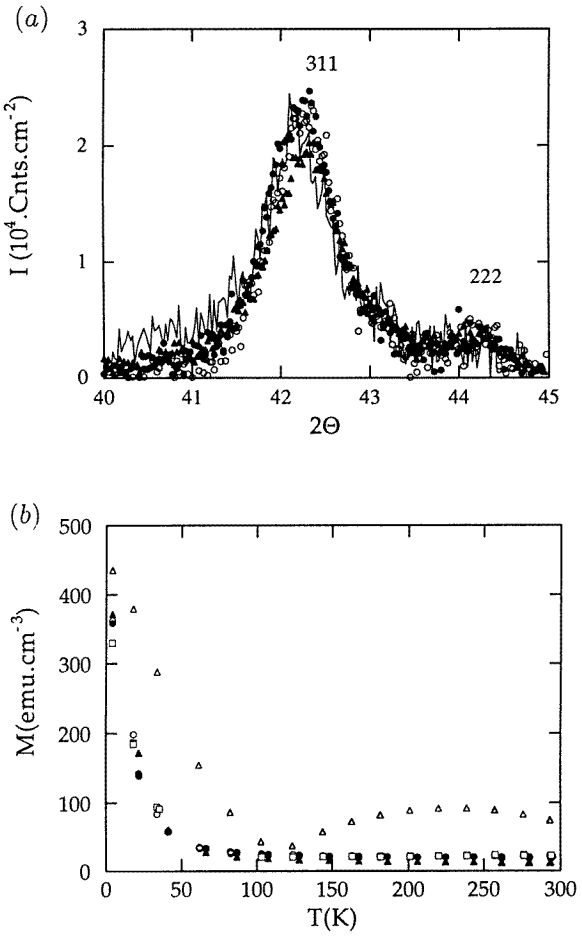

Figure 7. (a) A detailed view of the $TmCo_2$ 311 and 222 reflections for the samples irradiated at 10^{12} ions cm^{-2} (full triangles), 5×10^{12} ions cm^{-2} (open circles) and 10^{13} ions cm^{-2} (full circles); compared to those of the non-irradiated sample (full line). (b) The thermal variation of the magnetization measured in a field $H = 10$ kOe for the as-deposited amorphous samples (open triangles), for the heat-treated crystalline samples (open squares) and for the samples irradiated at 10^{12} ions cm^{-2} (full triangles), 5×10^{12} ions cm^{-2} (open circles) and 10^{13} ions cm^{-2} (full circles).

3.5. $TmCo_2$

The as-deposited amorphous samples are ferrimagnetic up to room temperature, with a compensation temperature 120 K (figure 7(b)). After crystallization, no compensation temperature is observed and the transition from the ferrimagnetic to the paramagnetic state is observed to occur at around 40 K (figure 7(b)).

The crystalline samples have been irradiated at room temperature by 5 GeV ^{208}Pb beams. Fluences of 10^{12}, 5×10^{12} and 10^{13} ions cm^{-2} have been achieved. Figure 7(a) shows a detailed view of the 311 and 222 reflections for the irradiated samples. The same reflections for the not irradiated sample are also shown for reference. No significant variation of the peak intensities is observed versus fluence.

Figure 7(b) shows the thermal variation of the magnetization measured in a constant field $H = 10$ kOe of the irradiated samples. With respect to the non-irradiated crystalline sample, no significant variation of the magnetic properties is observed. These results show that no amorphization has been induced by irradiation.

4. Thermal spike calculations

In the previous section it has been shown that heavy-ion irradiation in the electronic stopping power regime (namely $S_e \gg S_n$) can induce structural modifications and amorphization in the metallic compounds R–Co. In the following, the experimental results are interpreted on the basis of a microscopic energy transfer mechanism, the thermal spike. The latent track diameters are determined in YCo_2, $CeCo_3$, YCo_3 and $CeCo_2$. The calculation could not be performed for the $TmCo_2$ compound because most of the required data are unknown.

According to the thermal spike model, the energy deposited by incident ions on the electron gas of a metal through electronic energy loss is subsequently transferred to the lattice by electron–phonon interaction [26]. Following previous papers, in which the thermal spike has been applied successfully to calculate the track diameters in some amorphous materials and pure metals [27–29], the process is assumed to be described by two coupled differential equations governing the energy diffusion in the two sub-systems (electrons and lattice) and their coupling. Such a description is supported by experiments on metals irradiated by femtosecond laser pulses, in which good agreement is found between the theory and experiments [30]. The thermal spike is expressed in cylindrical symmetry, since radiation defects created in materials by highly energetic ions are cylindrical:

$$C_e(T_e)\frac{\partial T_e}{\partial t} = \frac{\partial}{\partial r}\left(K_e(T_e)\frac{\partial T_e}{\partial r}\right) + \frac{K_e(T_e)}{r}\frac{\partial T_e}{\partial r} - g(T_e - T_a) + A(r,t) \quad (4a)$$

$$C_a(T_a)\frac{\partial T_a}{\partial t} = \frac{\partial}{\partial r}\left(K_a(T_a)\frac{\partial T_a}{\partial r}\right) + \frac{K_a(T_a)}{r}\frac{\partial T_a}{\partial r} + g(T_e - T_a) \quad (4b)$$

where $A(r,t)$ is the energy density per unit time supplied by the incident ions to the electronic system at radius r and time t such that

$$\iint A(r,t)2\pi r \,\mathrm{d}r \,\mathrm{d}t = S_e \quad (5)$$

where g is the phenomenological electron–phonon coupling constant; and C_e, K_e, C_a and K_a are the specific heats and the thermal conductivities for the electrons and the lattice respectively.

The numerical solution of the system (4) allows the lattice temperature $T_a(r,t)$ at each time t and radius r to be calculated. It is assumed that the latent track results from rapid quenching of a cylinder of molten matter. Therefore, the latent track diameter is taken as the diameter of the biggest cylinder for which the lattice temperature T_a becomes higher than the melting temperature T_f. The latent heat of fusion is taken into account.

C_e and K_e have been calculated in the framework of the free-electron model, as in [27, 28]. In the following, the main assumptions that we have made in order to calculate the atomic lattice parameters are discussed and the results of the thermal spike calculations are presented.

4.1. Thermal conductivity

To the best of our knowledge, the thermal conductivity of the compounds under study has never been measured. For each compound we have thus calculated K_a at room temperature

from the resistivity values assuming the Wiedemann–Franz law to be valid, as in [28]. For the room-temperature resistivity we have taken the values reported in the literature for polycrystalline bulk samples [31, 32]. The values of the residual resistivity given in [32] for YCo_3 and $CeCo_3$ are abnormally high, probably because of the poor quality of the samples (as stressed by the authors). Thus, we have taken the room-temperature values obtained after scaling the residual resistivities to the values of YCo_2 and $CeCo_2$, by applying the Mathiessen rule, which is followed by intermetallic compounds [31].

4.2. The specific heat and energy required to melt the compounds

The thermal variation of the specific heat of YCo_2 has been measured by Voiron between 4 K and room temperature [33]. Similar measurements could not be found in the literature for the other compounds. Hence we have supposed the Dulong–Petit law to be followed by these compounds. This assumption is reasonable if one considers that the measured value 2.6 J cm^{-3} K^{-1} at room temperature for YCo_2 is in good agreement with the value of 2.8 J cm^{-3} K^{-1} deduced from the Dulong–Petit law.

The energy required to melt can be estimated as [28]

$$E_m = C_s(T_f - T_i) + \Delta H_f \tag{6}$$

where C_s is the specific heat, T_f is the melting temperature, T_i is the initial lattice temperature and ΔH_f is the latent heat of fusion. The latent heat of fusion for a compound X_aY_b can be expressed as [34]

$$\Delta H_f = \Delta H_{mix}^{liq} + a\Delta H_f(X) + b\Delta H_f(Y) - \Delta_f H. \tag{7}$$

The first term in equation (7) is the mixing enthalpy in the liquid state between the two elements constituting the compound; $\Delta H_f(X)$ and $\Delta H_f(Y)$ are the latent heats of the two individual elements constituting the compound and $\Delta_f H$ is the enthalpy of formation of the compound. The mixing enthalpies in the liquid state for YCo_2 and YCo_3 have been measured by Sidorov *et al* [35]. In contrast, such values are unknown for $CeCo_2$ and $CeCo_3$. The experimental values of $CeCu_2$ and $CeCu_3$ [36] have been used in the present calculation. In fact, measurements performed on intermetallic compounds constituted by the other rare earths with copper, nickel, iron and cobalt show that the values which best approximate the ΔH_{mix}^{liq} values of the R–Co compounds are those of R–Cu [34].

Latents heats of the individual elements were taken from [37]; those of the enthalpy of formation from [34]. The energy required to melt the compounds is reported in table 1.

4.3. The electron–phonon coupling constant g

The following *ad hoc* expression for the electron–phonon coupling constant g has been derived [28] for use in thermal spike calculations:

$$g \propto \frac{\Theta_D^2 n_e^2}{K_a n_a^{2/3}} \tag{8}$$

where n_e is the electronic density, Θ_D is the Debye temperature, K_a is the thermal conductivity of the lattice and n_a is the atomic density. By applying the Wiedemann–Franz law, equation (8) becomes

$$g \propto \frac{\Theta_D^2 n_e^2 \rho}{n_a^{2/3} L_0 T} \tag{9}$$

Table 1. The main parameters used in thermal spike calculations.

	YCo_2	$CeCo_3$	YCo_3	$CeCo_2$
ρ (300 K) ($\mu\Omega$ cm)	162	550	300	105
Θ_D (K)	300	273	332	246
g (300 K) (10^{12} W K^{-1} cm^{-3})	1.9	6.0	4.8	0.9
E_m (J cm^{-3})	9792	12 186	13 363	8691
T_f (K)	1427	1376	1583	1309
E_{ion} (MeV A^{-1})	3.7	24	24	24
S_e (KeV Å^{-1})	5.50 (SME-U)	4.44 (HE-Pb)	4.43 (HE-Pb)	4.25 (HE-Pb)

Table 2. Comparison between the experimental values of the Debye temperatures of some intermetallic compounds [24] and those calculated by scaling the YCo_2 Debye temperature with equation (10). Experimental errors were not given in the references.

	Θ_D(exp) (K)	Θ_D(calc) (K)
YNi_3	335	337
$LuAl_2$	269	272
YNi_2	291	317
$HoCo_2$	270	263
$GdNi_2$	266	237

Table 3. A comparison between experimental and calculated values of the track diameters. Because of the small number of experimental points the track diameter for YCo_3 could not be exactly determined (see section 3). However, by considering the fact that the measured $p_a(\Phi)$ values are of the same order of magnitude as those found for YCo_2 and $CeCo_3$, it is reasonable to expect the track diameter to be in the same range.

	D_1(exp) (Å)	D_1(calc) (Å)
YCo_2	21 ± 0.5	20
YCo_3		20
$CeCo_2$	0	0
$CeCo_3$	30 ± 3	60

where $L_0 = 2.45 \times 10^{-8}$ W Ω K^{-2} is the Lorenz number and ρ is the electrical resistivity. The electronic density n_e has been evaluated as $n_e = z\ n_a$, where z [38] has been taken as the weighted average of the valence of the individual elements constituting the alloy (z(Co) = 2, $z(Y) = 3$ and z(Ce) = 3.5). g has been determined with equation (9) at room temperature for all the compounds (table 1).

Only the YCo_2 Debye temperature is known experimentally ($\Theta_D = 300$ K) [33]. In the present calculation, the Debye temperatures of the other compounds were determined

by scaling the YCo_2 Debye temperature with the Lindemann criterion. The Lindemann criterion is written as [39]

$$\Theta_D \propto \left(\frac{T_f n_a^{2/3}}{PA}\right)^{1/2} \tag{10}$$

where T_f is the melting temperature (table 1), n_a the atomic density and PA the atomic weight. Equation (10) has been applied to the compounds considered here, after substituting for the atomic weight the average atomic weight of each alloy.

We have tested this criterion for the rare earth–transition metal intermetallic compounds, whose Θ_D values have been determined experimentally. Table 2 shows the results obtained by using equation (10), compared to the experimental values taken from [24]. The agreement between experimental and calculated values is reasonable.

In this calculation, we have considered the YCo_2 alloy and then determined the coupling constant g which reproduced the track diameter found experimentally. The values of g for the other compounds were determined by scaling the g value found for YCo_2 with equation (9). Table 1 shows the values of the main parameters used in the calculation.

4.4. Results

Figure 8 shows the lattice temperature versus time calculated for all the compounds at different distances from the heavy-ion path (which has been taken as the axis of the cylindrical coordinate system). The latent track radius is taken equal to the largest radius for which $T_a > T_f$, namely equal to the radius of the largest cylinder which melts. In table 3 the calculated diameters are compared with the diameters determined experimentally in the previous section. Good qualitative agreement is found.

A similar behaviour is obtained for YCo_2, YCo_3 and $CeCo_3$, in agreement with x-ray diffraction and magnetic measurements. On the other hand, the $CeCo_2$ lattice is heated up to the melting temperature, but no solid–liquid transformation occurs. It follows that this alloy can be considered to be on the verge of damage, in agreement with the experimental observation of modifications of the crystalline structure without amorphization.

These results indicate that samples with the same microstructure and similar electronic properties can behave differently when irradiated by swift heavy-ions because of different lattice properties. According to the present calculation, in agreement with the experimental results, the main parameter determining the sensitivity of a material is the electron–phonon coupling constant g. In this respect, $CeCo_2$ is particularly interesting since it requires less energy to melt it than do the other compounds, but it is not amorphized by irradiation. This is mainly because $CeCo_2$ has a weaker electron–phonon coupling than do the other compounds.

5. Conclusion

RCo_2 (R = Y, Ce and Tm) and RCo_3 (R = Y and Ce) intermetallic compounds have been prepared by sputter deposition and subsequent heat treatment in the form of isotropic polycrystalline films. They were irradiated at GANIL (Caen, France) either by 1 GeV U or 5 GeV Pb ion beams. The irradiation-induced damage was investigated by x-ray diffraction and magnetic measurements. The experimental results can be summarized as follows.

(i) YCo_2, $CeCo_3$ and YCo_3 have been found to be partially amorphized. The amorphized volume fractions saturate before complete amorphization of the sample is achieved. In order to explain such a behaviour a phenomenological model associating amorphization and

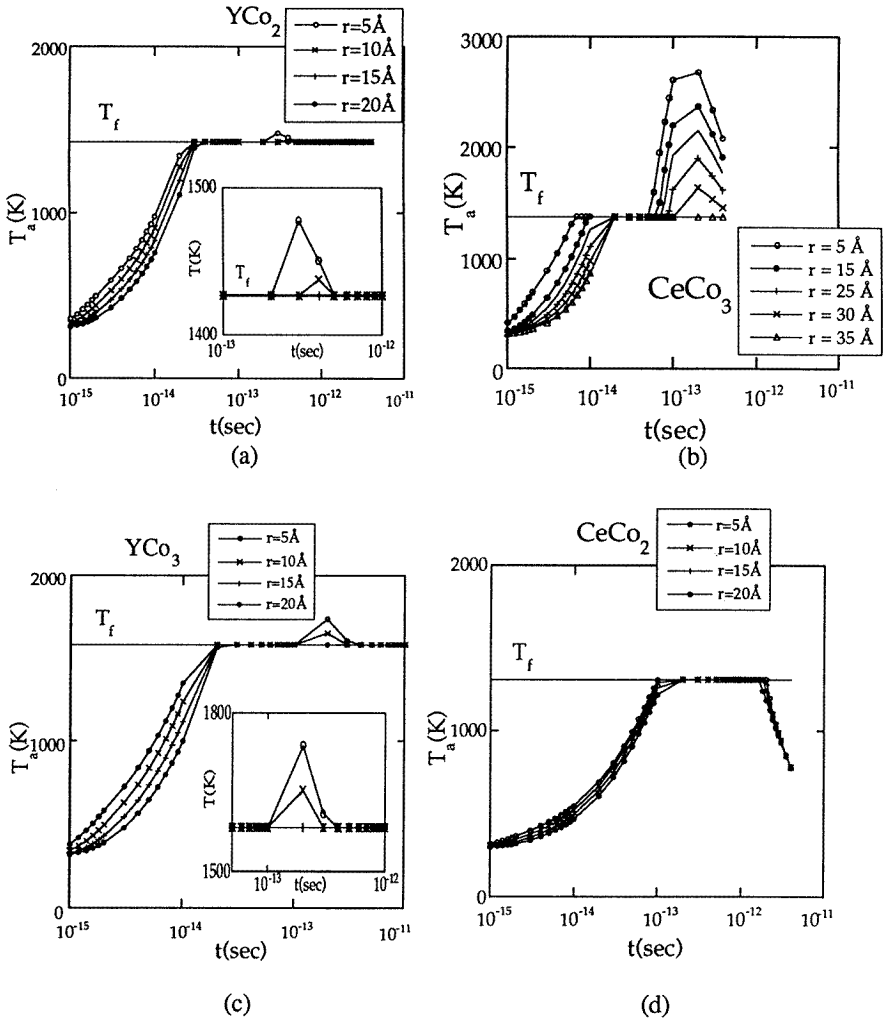

Figure 8. (a) The lattice temperature versus time for YCo_2 at different distances from the heavy-ion path (taken as the axis of the cylindrical coordinate system); (b) The lattice temperature versus time for $CeCo_3$. (c) The lattice temperature versus time for YCo_3. (d) The lattice temperature versus time for in $CeCo_2$. The horizontal full lines refer to the melting points.

recrystallization has been developed. The track diameters are estimated to lie within the range 2–3 nm.

(ii) No amorphization was induced in $CeCo_2$. Modifications of the crystal structure are observed, which could be associated with the stabilization of a new crystallographic phase, which could not be identified. Further investigation is required.

(iii) Neither amorphization nor structural modifications are observed in $TmCo_2$.

The thermal spike model has been applied to YCo_2, $CeCo_3$, YCo_3 and $CeCo_2$. The calculation could not be performed for $TmCo_2$, since most of the needed parameters were unknown. The latent track diameters have been calculated and were found to be in quali-

tative agreement with experiment. The results indicate that the sensitivity of a material to heavy-ion irradiation is mainly determined by the intensity of its electron–phonon coupling.

References

[1] Balanzat E 1993 *Radiat. Eff.* **126** 97
[2] Iwase A, Sazaki S, Iwata T and Nihira T 1987 *Phys. Rev. Lett.* **58** 2450
[3] Dunlop A, Lesueur D, Morillo J, Dural J, Spohr R and Vetter J 1989 *C.R. Acad. Sci. Paris* **309** 1277
[4] Dunlop A and Lesueur D 1993 *Radiat. Eff.* **126** 123
[5] Legrand P, Dunlop A, Lesueur D, Lorenzelli N, Morillo J and Bouffard S 1992 *Mater. Sci. Forum* **97–99** 587
[6] Henry J, Barbu A, Leridon B, Lesueur D and Dunlop A 1992 *Nucl. Instrum. Methods.* B **67** 390
[7] Barbu A, Dunlop A, Henry J, Lesueur D and Lorenzelli N 1992 *Mater. Sci. Forum* **97–99** 577
[8] Audouard A, Balanzat E, Bouffard S, Jousset J C, Chamberod A, Dunlop A, Lesueur D, Fuchs G, Spohr R, Vetter J and Thomé L 1990 *Phys. Rev. Lett.* **65** 875
[9] Barbu A, Dunlop A, Lesueur D and Averback R S 1991 *Europhys. Lett.* **15** 37
[10] Ghidini M 1995 *Thèse de doctorat* Université J Fourier, Grenoble
[11] Farrow R F C *et al* (eds) 1993 *Magnetism and Structure in Systems of Reduced Dimensions* (New York: Plenum)
Davies H 1994 Ultrafine Alloys make their mark *Physics World* November 40
[12] Givord D, Nozières J P, Ghidini M, Gervais B and Otani Y 1994 *J. Appl. Phys.* **76** 6661
[13] Ghidini M, Nozières J P, Givord D and Gervais B 1995 *J. Magn. Magn. Mater.* **140–144** 483
[14] Givord D, Nozières J P, Ghidini M, Gervais B and Otani Y 1995 *J. Magn. Magn. Mater.* **148** 253
[15] Ziegler J F, Biersack J P and Littmark U 1985 *Stopping Power and Ranges of Ions in Matter* ed J F Ziegler (New York: Pergamon)
[16] Moorjani K and Coey J M D 1984 *Magnetic Glasses* ed S P Wohlsky and A W Czaderna (Amsterdam: Elsevier)
[17] Suran G, Ghidini M and Nozières J P to be published
[18] Ghidini M, Nozières J P, Givord D, Liénard A, Gervais B and Doorhyèe E 1996 *Nucl. Instrum. Methods* B **107** 344
[19] Albrecht D, Armbruster P, Spohr R, Roth M, Schaupert K and Stuhrmann H 1985 *Appl. Phys.* A **37** 37
[20] Dartyge E, Lambert M and Maurette M 1976 *J. Physique* **37** 939
[21] Malterre D, Durand J, Siari A and Marchal G 1988 *J. Physique* **49** C8 1359
[22] Lemaire R *et al* 1967 *J. Phys. Chem. Solids* **28** 2471
[23] Ghidini M, Nozières J P and Givord D to be published
[24] Burzo E, Chelkowski A and Kirchmayr H R *Magnetic Properties of Metals* vol 2, ed H P J Wijn (Berlin: Springer)
[25] Longworth G and Harris I R 1975 *J. Less-Commom. Met.* **41** 175
[26] Seitz F and Koehler J S 1956 *Solid State Physics* vol 2 (New York: Academic)
[27] Toulemonde M, Dufour C and Paumier E 1992 *Phys. Rev.* B **46** 14 362
[28] Wang Z G, Dufour C, Paumier E and Toulemonde M 1994 *J. Phys.: Condens. Matter* **6** 6733
[29] Toulemonde M, Paumier E and Dufour C 1993 *Radiat. Eff.* **126** 201
[30] Brorson S D, Kazeroonian A, Moodera J S, Face D W, Cheng T K, Ippen E P, Dresselhaus M S and Dresselhaus G 1990 *Phys. Rev. Lett.* **64** 2172
[31] Gratz E and Zuckermann M J 1982 *Handbook on the Physics and Chemistry of Rare Earths* vol 5, eds K A Gscheidner and L R Eyring (Amsterdam: North-Holland)
[32] du Plessys P V and Germishuyse T 1992 *J. Magn. Magn. Mater.* **104–107** 1349
[33] Voiron J 1973 *Thèse*, Université Scientifique et Medicale, Grenoble
[34] Colinet C 1995 Private communication
Colinet C and Pasturel A 1994 Thermodynamic Properties of Metallic Systems *Handbook on the Physics and Chemistry of Rare Earths* vol 19, ed K A Gschneidner *et al* (Amsterdam: Elsevier)
[35] Sidorov O Y, Esin Y O, Geld P V and Kirova S M 1988 *Rasplavy* **2** 101
[36] Fitzner and Kleppa 1994 *Metall. Mater. Trans.* A **25** 1495
[37] *Handbook of Physics and Chemistry* (Boca Raton, FL: CRC)
[38] Ashcroft N W and Mermin M D 1976 *Solid State Physics* (New York: Addison-Wesley)
[39] Pines D 1963 *Elementary Excitations in Solids* (New York: Addison-Wesley)